Journal of Agricultural Engineering

https://www.agroengineering.org/

Safety-refined and smoothness-enhanced path-planning algorithm for an agricultural composite mobile manipulator in greenhouse crate handling

Haoxuan Hu, Chunyan Zhang

Shanghai University of Engineering Science, Shanghai, China

Corresponding author: Chunyan Zhang, Shanghai University of Engineering Science, Shanghai 201620, China. E-mail: cyzhang@sues.edu.cn

Please cite this article as doi: 10.4081/jae.2026.2024

Submitted: 29 October 2025
Accepted: 19 May 2026

Safety-refined and smoothness-enhanced path-planning algorithm for an agricultural composite mobile manipulator in greenhouse crate handling

Haoxuan Hu, Chunyan Zhang

Shanghai University of Engineering Science, Shanghai, China

Corresponding author: Chunyan Zhang, Shanghai University of Engineering Science, Shanghai 201620, China. E-mail: cyzhang@sues.edu.cn

CRediT authorship statement: Haoxuan Hu, conceptualization, software (SR-RRT-APF algorithm), writing – original draft. **Chunyan Zhang**, supervision, formal analysis, writing – review & editing. All authors read and approved the final version of the manuscript.

Conflict of interest: the authors declare no competing interest and all authors confirm accuracy.

Data availability statement: All data generated or analyzed during this study are available from the corresponding author upon reasonable request.

Abstract

With the growing demand for automation in greenhouse logistics, ensuring both operational safety and motion smoothness has become a key challenge for composite mobile manipulators working in confined agricultural environments. This study proposes a safety-refined and smoothness-enhanced path-planning algorithm, termed SR-RRT-APF, to improve path feasibility and collision avoidance for agricultural robotic systems. The method integrates scheduled goal biasing, curvature-aware parent-node selection, density-adaptive step sizing, and potential-field-based soft guidance into an improved RRT framework. By incorporating explicit minimum-clearance constraints and lightweight post-processing, the algorithm jointly optimizes safety margins and geometric smoothness during the path generation stage. Extensive simulations and prototype-level tests were conducted on a greenhouse crate-handling robot equipped with a 6-DOF manipulator and a vision-guided mobile chassis. Ten consecutive crate-handling cycles were performed, in which the robot autonomously recognized, grasped, transported, and placed vegetable crates within narrow greenhouse aisles. Results from the simulation benchmarks show that SR-RRT-APF achieves superior path quality, larger safety margins, and improved smoothness compared with the benchmark algorithms in dense and constrained workspaces. Prototype-level experiments on a greenhouse crate-handling robot further support the system-level feasibility of the associated perception–manipulation workflow,

indicating the practical relevance of the proposed method in greenhouse operations while also suggesting its applicability to a broader class of constrained-space planning problems.

Key words: artificial potential field; automated greenhouse logistics; composite mobile manipulator; industrial automation; path planning; RRT algorithm.

Introduction

With the continuous advancement of smart agriculture and unmanned farming, the demand for automation in greenhouse operations has rapidly increased. Composite mobile robots that integrate a mobile chassis and a multi-degree-of-freedom manipulator have become essential for tasks such as harvesting, sorting, and crate handling (Sun and Yi, 2023; Gao *et al.*, 2023; Zhu *et al.*, 2024. However, compared with structured industrial environments, agricultural settings are typically unstructured, cluttered, and spatially constrained. Dense plant rows, narrow aisles, and irregular obstacles impose stricter requirements on the robot's motion safety, trajectory smoothness, and operational reliability (Sánchez-Molina *et al.*, 2024; Rajendran *et al*., 2024). From an algorithmic perspective, sampling-based motion planning has become a cornerstone of robotic navigation and manipulation owing to its scalability and low dependence on explicit environment modeling. Among these methods, the Rapidly-Exploring Random Tree (RRT) and its derivatives -such as RRT-Connect (Kuffner and LaValle, 2000), Informed RRT* (Gammell *et al.,* 2022), and Halton-sequence-based RRT (HB-RRT) (Zhong *et al*., 2024)- have been widely employed in both mobile and manipulator path planning. Over the past two decades, improvements to the RRT family have evolved along several conceptual directions.

First, research on sampling-distribution optimization has focused on achieving faster convergence and more uniform search coverage through techniques such as low-discrepancy or adaptive goal-biased sampling, Halton or Sobol sequences, and informed ellipsoidal sampling (Gammell *et al*., 2022; Zhong *et al.,* 2024; Liu *et al*., 2023). These approaches can accelerate the discovery of feasible paths in complex or high-dimensional spaces but often neglect curvature continuity and local executability. Second, studies on expansion and local-cost optimization have introduced adaptive step-length control and curvature-aware parent-node selection to improve geometric smoothness and path stability (Lin and Zhang, 2024; Zhang et *al*., 2024; Huang *et al*., 2025). These methods reduce sharp directional changes and enhance

trajectory quality but may still lack explicit safety modeling, especially in densely cluttered environments where minimum clearance is critical for collision-free motion. Third, safety-constrained and potential-field integration methods have attracted extensive attention. The Artificial Potential Field (APF) approach provides continuous attractive and repulsive forces for obstacle avoidance and local trajectory smoothing. Its integration with RRT has led to various hybrid variants -such as improved RRT-APF (Zhang *et al.*, 2024), AODA-PF-RRT* (Wang *et al.*, 2024), DBVS-APF-RRT* (Feng *et al.*, 2024), and bi-directional APF-RRT* (Lin *et al.*, 2023)- which effectively improve obstacle avoidance and path regularity. Recent studies have also combined potential-field modulation with penalty functions (Bian *et al.*, 2023) or reweighted cost terms (Zhang *et al.*, 2025) to further enhance feasibility. Nevertheless, most existing RRT–APF hybrids rely on empirical tuning and treat safety or smoothness as post-processing objectives rather than as embedded generation constraints.

In the context of agricultural robotics, RRT-based algorithms have been adapted to orchard and greenhouse environments, where improved RRT-Connect or RRT* frameworks demonstrated shorter paths and more stable planning times for manipulators operating under dense foliage or narrow inter-row conditions (Chen *et al.*, 2022; Li and Ma, 2023; Lu *et al.*, 2024; Wei *et al.*, 2025). However, these adaptations generally depend on environment-specific parameters and lack explicit mechanisms to guarantee minimum clearance or enforce curvature continuity. As a result, the generated trajectories may exhibit local zigzagging, boundary-skimming behaviors, or insufficient safety margins —issues that critically limit the deplorability of robotic arms carrying large crates within confined aisles. To address these limitations, this study develops a Safety-Refined Rapidly-Exploring Random Tree with Artificial Potential Field (SR-RRT-APF) algorithm for narrow and obstacle-dense constrained workspaces, with greenhouse crate handling serving as the primary application motivation and validation scenario. To address these limitations, this study develops a Safety-Refined Rapidly-Exploring Random Tree with Artificial Potential Field (SR-RRT-APF) algorithm for narrow and obstacle-dense constrained workspaces, with greenhouse crate handling serving as the primary application motivation and validation scenario. Unlike conventional RRT-APF hybrids that rely heavily on post-generation smoothing, the proposed method introduces safety- and smoothness-aware guidance during sampling, expansion, and lightweight final refinement. The algorithm is quantitatively

evaluated through simulation benchmarks and further examined on a self-developed greenhouse robot platform to verify the system-level feasibility of the associated perception-manipulation workflow.

The main contributions of this research are summarized as follows: i) A unified safety–smoothness path-generation framework. A novel SR-RRT-APF algorithm is developed by embedding safety and curvature constraints directly into the sampling and expansion phases of RRT. Unlike conventional planners that rely primarily on post-processing smoothing, this design introduces safety and smoothness considerations during the tree-generation stage, enabling the planner to simultaneously maintain collision avoidance and geometric continuity throughout the planning process. ii) Explicit minimum-clearance modeling and density-adaptive expansion strategy. A mathematically defined minimum-clearance constraint is incorporated into both the expansion and post-processing stages. Combined with the proposed obstacle-density–adaptive step-length mechanism, the planner dynamically regulates exploration aggressiveness according to local environmental complexity while maintaining sufficient safety margins. iii) Lightweight safety-aware trajectory refinement module. Two lightweight refinement operators -clearance-constrained shortcutting and normal-direction push-away adjustment- are introduced to improve trajectory compactness and stability while preserving path feasibility and safety margins. iv) Comprehensive simulation evaluation and system-level experimental validation. The proposed SR-RRT-APF planner is evaluated through extensive simulations under multiple obstacle-density configurations and a narrow-passage scenario, and further assessed on a self-developed agricultural robotic platform to demonstrate system-level feasibility. Compared with representative planners including RRT-Connect, AI-RRT, and APF-RRT*-Ji, the proposed method consistently generates smoother trajectories with significantly fewer turning points and larger safety clearances. In dense and constrained environments, SR-RRT-APF reduces path length by approximately 25–30% relative to RRT-Connect, decreases the number of turning points by about 80–95%, and increases the minimum obstacle clearance by up to approximately three times, while maintaining competitive computation time.

Overall, the SR-RRT-APF algorithm establishes a mathematically grounded and experimentally verified framework for safety-refined motion planning in narrow and obstacle-dense

agricultural environments.

Problem definition and agricultural application background

Compared with industrial production lines, greenhouse environments are typically unstructured, densely cluttered, and spatially constrained within narrow aisles (Zhao *et al.*, 2022; Liu *et al.*, 2023; Zhang *et al.*, 2025). The major obstacles include structural pillars and beams of the greenhouse, the boundaries of the mobile chassis, and the edges of inter-row passages. Under such spatial constraints, a path-planning algorithm must not only guarantee connectivity between the start and goal configurations but also preserve sufficient safety margins to prevent any interference or collision between the robot arm and its surroundings.

The workspace of the robot arm's end effector is modeled as a subset $\Omega \subseteq \mathbb{R}^d, d \in \{2,3\}$, representing all reachable positions. The environment contains several approximately spherical obstacles, each characterized by its center c_i and r_i. To account for the physical envelope of the robot arm and its payload, a minimum safety margin $s$is introduced, where $s$represents the minimum allowable clearance between the robot envelope and surrounding obstacles during motion. Accordingly, the effective radius of each obstacle is expanded to $r_i + s$.

Accordingly, the configuration space can be divided into two regions, as formulated in Eqs. (1) and (2):

$$\Omega_{\text{forb}} = \{ x \in \Omega \mid \min_i \| x - c_i \| < r_i + s \} \quad \text{(Eq. 1)}$$

where $\| x - c_i \|$denotes the Euclidean distance between any point $x$and the center $c_i$of the i-th obstacle.

$$\Omega_{\text{free}} = \Omega \setminus \Omega_{\text{forb}} \quad \text{(Eq. 2)}$$

which defines all admissible positions of the end effector without collision.

Given a start point x_s and a goal point x_g in the robot-base coordinate frame, the path-planning objective is to search for a continuous curve

$$\gamma: [0,1] \to \Omega_{\text{free}}, \quad \text{(Eq. 3)}$$

satisfying the boundary conditions

$$\gamma(0) = x_s, \gamma(1) = x_g, \quad \text{(Eq. 4)}$$

that minimizes the geometric path length

$$J(\gamma) = \int_0^1 \| \dot{\gamma}(t) \| \, dt, \quad \text{(Eq. 5)}$$

where $\dot{\gamma}(t)$ is the instantaneous velocity vector along the path.

Meanwhile, every point on the path must obey a *pointwise safety constraint* ensuring a minimum clearance from obstacles:

$$\mathrm{clr}(x) = \min_i (\| x - c_i \| - r_i) \geq s, \qquad \text{(Eq. 6)}$$

where $clr(x)$ represents the shortest distance between point $x$and the nearest obstacle surface, and $s$defines the required minimum safety clearance.

Figure 1 provides a geometric interpretation of these formulations in the context of greenhouse crate-handling operations. Panels (a) to (c) correspond to the grasping, handling, and placing phases, respectively, illustrating how the end effector moves relative to the chassis, the loading platform, and surrounding obstacles within narrow aisles. The region Ω_{forb} denotes the forbidden space, while Ω free defines the feasible workspace of the manipulator. During motion, the effective obstacle radius $r_i + s$ forms an outer safety envelope within which the trajectory γ(t) must remain so that $\min_t$ clr $(\gamma(t)) \geq s$.

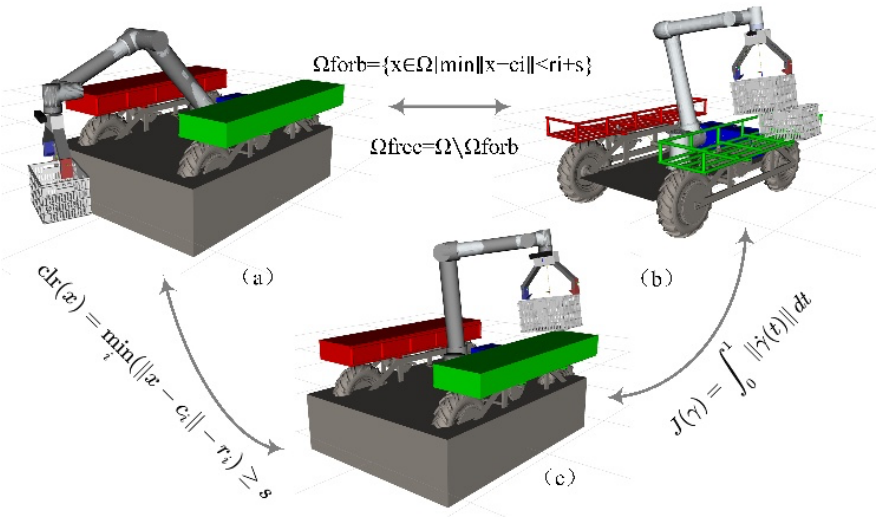

Figure 1. Mathematical formulation of the path-planning problem.

At the placing stage, where the end effector approaches the pallet boundary $\mathrm{clr}(x) = \mathrm{s}$, the cost function $J(\gamma)$ represents the shortest feasible trajectory under the given safety constraint. This modeling framework establishes the mathematical foundation for the subsequent SR-RRT-APF algorithm, in which the minimum-clearance constraint (Eq. 6) is embedded directly into the path-generation process to ensure collision-free and geometrically continuous motion in greenhouse environments.

In summary, the path-planning problem can be formally defined as searching, within the free

space Ω_{free}, for an optimal curve $\gamma(t)$ that satisfies the minimum-clearance constraint $clr(x) \geq s$while minimizing the geometric path length $J(\gamma)$.

The overall workflow of SR-RRT-APF, illustrated in Figure 2, follows a unified generation–refinement pipeline that transforms conventional RRT–APF hybrids into a constraint-driven framework. During the sampling phase, the algorithm employs a dynamically scheduled goal-bias probability $p_g(k)$ to balance exploration and exploitation, and activates informed ellipsoidal sampling once a feasible upper bound $c_{best}$is obtained, thereby focusing the search within promising regions. Once an initial feasible path is discovered, the current best cost c_{best}defines the informed ellipsoid, and subsequent samples are drawn from this region while the tree continues to expand during later iterations. The safety-constrained post-processing procedure is executed only once after the planning process terminates and the final path has been extracted, rather than being applied after each sampling iteration.

Each candidate sample is subsequently refined through artificial potential-field modulation, where adaptive attractive and repulsive forces based on target distance and obstacle density guide the sampling process toward safer and more directed configurations.

In the tree-expansion phase, SR-RRT-APF introduces a curvature-aware parent-node selection strategy that combines Euclidean distance and turning-angle cost, ensuring locally smooth growth and suppressing abrupt directional changes. The expansion step length is further adjusted according to local obstacle density to maintain a minimum-clearance constraint $d_{min} \geq \delta$, guaranteeing segment-level geometric feasibility. Once the target node is connected, the least-cost trajectory is extracted through backtracking, and a lightweight refinement procedure—comprising clearance-constrained shortcutting and normal-direction push-away correction—enhances safety margins and continuity without altering the overall topology of the path.

During the search process, whenever a lower-cost path is discovered, the cost bound $c_{best}$is updated and used to restrict subsequent sampling within the informed ellipsoid. Through this integrated process, SR-RRT-APF jointly optimizes safety and smoothness under explicit mathematical constraints, providing a robust and theoretically grounded alternative to conventional heuristic RRT–APF methods.

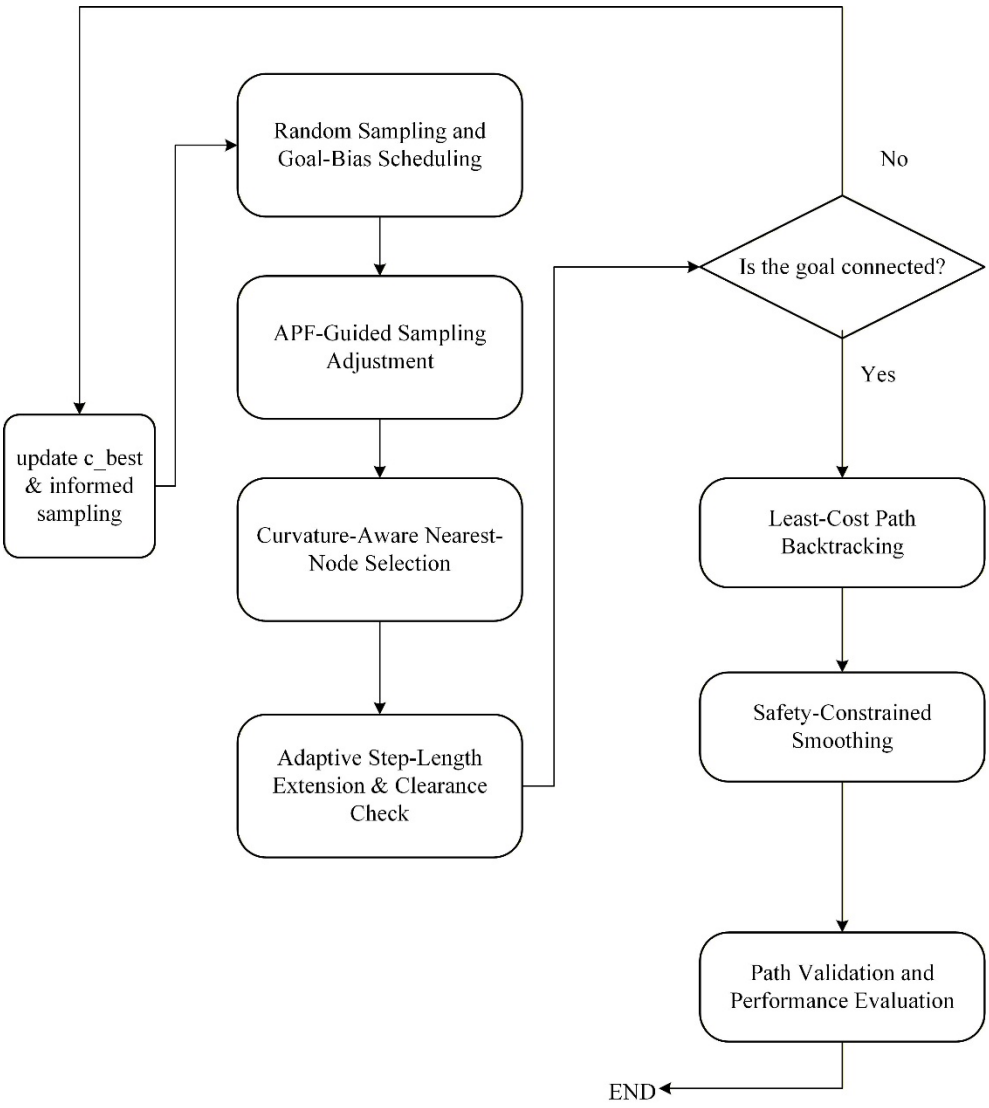

Figure 2. Workflow of the proposed SR-RRT-APF algorithm.

Materials and Methods

SR-RRT-APF algorithm

Sampling and guidance mechanism

In greenhouse agricultural operations, the workspace is narrow, cluttered, and irregularly distributed with obstacles. Conventional random sampling often leads to redundant exploration or premature convergence near obstacles, compromising both efficiency and safety. To overcome these issues, the SR-RRT-APF algorithm incorporates a safety-constrained sampling guidance mechanism that embeds directional and clearance awareness directly into the

sampling process, ensuring balanced tree expansion and adequate safety margins from the onset of planning.

To smoothly transition from global exploration to rapid convergence, the algorithm jointly employs scheduled goal-bias sampling and Informed Ellipsoidal Sampling at each iteration k. A dynamic artificial potential field (APF) is further superimposed on the sampling process to integrate both goal-oriented guidance and safety awareness. The adaptive goal-bias probability $p_g(k)$ evolves according to

$$p_g(k) = P_0 + (P_{\max} - P_0)(1 - e^{-\frac{k}{\tau}}), 0 < P_0 < P_{\max} < 1 \quad \text{(Eq. 7)}$$

where τcontrols the rate of transition from exploration to exploitation.

Once a feasible path of length $c_{best}$is found, sampling is conditionally refined within an ellipsoidal domain whose foci correspond to the start $x_s$and goal x_g. The ellipsoid center is $c = \frac{1}{2}(x_s + x_g)$, with major and minor semi-axes $a = c_{best}/2$and $b = \sqrt{a^2 - (\| x_g - x_s \|/2)^2}$, respectively. Its principal axis aligns with the vector $x_g - x_s$through a rotation matrix R, giving the sampling equation

$$x = c + R \cdot \mathrm{diag}(a, b, b) \cdot v, \| v \| \leq 1. \quad \text{(Eq. 8)}$$

where $v$is a random vector uniformly sampled from the interior of a unit-radius hypersphere, i.e., $v \sim \mathcal{U}(B_n(0,1))$. This formulation follows the informed ellipsoidal sampling strategy commonly adopted in Informed RRT to improve sampling efficiency after an initial feasible solution is obtained (Gammell *et al.*, 2022). The point $x$generated by Eq. (8) represents the raw candidate sample before potential-field modulation.

If no feasible path exists, the process degenerates to uniform random sampling, preserving the probabilistic completeness of the algorithm.

To simultaneously strengthen goal attraction near the target and enhance obstacle repulsion in dense regions, each candidate sample $\tilde{x}$is iteratively adjusted by a combined attractive–repulsive force field.

The attractive and repulsive components are formulated as

$$F_{\text{att}}(\tilde{x}, k) = \epsilon(\tilde{x}, k) \cdot (x_g - \tilde{x}), F_{\text{rep}}(\tilde{x}) = \sum_i \varphi_i(\tilde{x}) \cdot \frac{\tilde{x} - c_i}{\|\tilde{x} - c_i\|} \quad \text{(Eq. 9)}$$

where $d_i = \| \tilde{x} - c_i \|$denotes the distance between the candidate and the i-th obstacle.

The short-range repulsive term is activated only when $d_i < \rho_0$:

$$\varphi_i(\tilde{x}) = \begin{cases} \sigma(\tilde{x})\left(\frac{1}{d_i} - \frac{1}{\rho_0}\right)\frac{1}{d_i^2}, & \text{if } d_i < \rho_0 \\ 0, & \text{otherwise} \end{cases} \quad \text{(Eq. 10)}$$

where ρ_0 is the influence radius of the obstacle. The dynamic gains $\epsilon(\tilde{x}, k)$ and $\sigma(\tilde{x})$ are defined as

$$\epsilon(\tilde{x}, k) = \epsilon_0 \left(1 - \frac{\min(\|\tilde{x} - x_g\|, D_{max})}{D_{max}}\right), \sigma(\tilde{x}) = \sigma_0(1 + \rho(\tilde{x})) \quad \text{(Eq. 11)}$$

where

$$D_{max} = \max_{x_i \in T} \| x_i - x_g \|. \quad \text{(Eq. 12)}$$

is the maximum Euclidean distance between the goal node x_g and the nodes currently contained in the search tree T. Therefore, $D_{\max}$ is not a predefined constant but a dynamically updated quantity that evolves with tree growth. In practice, it can be updated incrementally when new nodes are inserted into the tree, with negligible computational cost relative to collision checking. Because $\min(\| \tilde{x} - x_g \|, D_{\max})/D_{\max} \in [0,1]$, the attractive gain remains bounded. Accordingly, the dependence of $\epsilon(\tilde{x}, k)$ on the iteration index k is implicit and arises through the evolution of the tree structure rather than through an explicit term on the right-hand side of Eq. (11), where $\rho(\tilde{x})$ denotes the local obstacle density within a neighborhood of radius R_ρ. In this study, the density is evaluated from the known environment map $world = \{(c_i, r_i)\}_{i=1}^{N}$, which specifies the positions and effective radii of all obstacles in the planning workspace. Specifically, the density at a candidate sample $\tilde{x}$ is defined as the normalized number of obstacles whose centers lie within the neighborhood centered at $\tilde{x}$:

$$\rho(\tilde{x}) = \frac{1}{N_\rho} \sum_{i=1}^{N} \mathbf{1}(\| \tilde{x} - c_i \| \leq R_\rho) \quad \text{(Eq. 13)}$$

where N_ρ is a normalization factor representing the maximum expected number of obstacles within the neighborhood, and $\mathbf{1}(\cdot)$ denotes the indicator function that equals 1 when the condition is satisfied and 0 otherwise. This formulation provides a quantitative measure of the spatial concentration of nearby obstacles. Regions with higher obstacle density lead to larger repulsive gains, thereby strengthening obstacle avoidance in cluttered areas, whereas sparse regions allow the planner to explore more directly toward the goal.

$$\tilde{x} \leftarrow \tilde{x} + \eta \cdot (F_{\text{att}}(\tilde{x}, k) + F_{\text{rep}}(\tilde{x})) \quad \text{(Eq. 14)}$$

Under the same collision-checking criterion consistent with the previously defined safety margin s, the micro-adjusted samples are passed to the subsequent tree-expansion stage for further processing. To ensure that the APF-based perturbation does not move the candidate sample outside the admissible planning domain, each adjusted point $\tilde{x}$is further subjected to a boundary-projection operation before tree expansion. Specifically, the function $project_to_world(\cdot)$maps the adjusted sample back into the predefined workspace Ωif it falls outside the world boundary defined by the obstacle set $world = \{(c_i, r_i)\}_{i=1}^{N}$. This operation effectively clips the sample to the nearest feasible position within the workspace, preventing invalid configurations caused by potential-field perturbations while preserving the probabilistic completeness of the sampling process.

This dynamic APF-based micro-adjustment mechanism enables SR-RRT-APF to adapt its sampling behavior to the dense and irregular obstacle distributions typical of greenhouse environments. By incorporating clearance and directional awareness into the sampling refinement step, the algorithm guides candidate samples toward safer and more directionally consistent configurations during tree expansion. This mechanism reduces the reliance on extensive post-processing while maintaining efficient exploration. Compared with existing hybrid planners such as BIAP-RRT (Bian *et al.*, 2023) and DCGB-DAPF-RRT* (Zhang *et al.*, 2025), the proposed method shows improved stability and efficiency in the tested greenhouse scenarios. The complete sampling and guidance mechanism is summarized in the pseudocode presented in Table 1.

Table 1. APF soft micro-adjustment for sampling points.

Algorithm 1.	
	Input: $k, x_s, x_g, c_{\text{best}}$,world $= \{(c_i, r_i)\}$,params $= \{P_0, P_{\max}, \tau, \epsilon_0, \sigma_0, \rho_0, R_\rho, \eta\}, d$
	Output: $\tilde{x}$
1.	$p_g = P_0 + (P_{\max} - P_0) \cdot (1 - \exp(-k/\tau))$
2.	$if\ rand(\ \ ) < p_g$:

3. $x = x_g$
4. $else\ if\ c_{\text{best}} < \infty$
5. $x = \text{informedSampling}(x_s, x_g, c_{\text{best}})$#Informed sampling
6. $else$
7. $x = \text{uniform\_sample(world)}$
8. $D_{\max} = \text{max\_distance\_to\_goal}(T, x_g)$
9. $\epsilon(x,k) = \epsilon_0 \cdot (1 - \frac{\|x - x_g\|}{D_{\max}})$
10. $\rho(x) = \text{obstacle\_density}(x)$
11. $\sigma(x) = \sigma_0 \cdot (1 + \rho(x))$
12. $F_{\text{att}} = \epsilon(x,k) \cdot (x_g - x)$
13. $F_{\text{rep}} = \text{sum of (repulsion forces from obstacles)}$
14. $\tilde{x} = x + \eta \cdot (F_{\text{att}} + F_{\text{rep}})$
15. $\tilde{x} = \text{project\_to\_world}(\tilde{x}, \text{world})$
16. $Returen\ \tilde{x}$

Core tree expansion

After the sampling and guidance phase in Section 2.1, the algorithm provides candidate samples that already carry directional bias and safety awareness. However, sampling alone is not sufficient to guarantee that the resulting trajectory will be executable. During expansion, SR-RRT-APF operates under the constraints of greenhouse manipulation: narrow inter-row spacing, complex unstructured surroundings, and limited clearance around a large-load composite mobile manipulator. The expansion policy therefore prioritizes the generation of geometrically continuous edges while explicitly enforcing a segment-level minimum-clearance constraint δ. In this way, path safety and smoothness are incorporated during tree growth rather than being handled only after path generation.

Curvature-aware nearest-node selection

In classical sampling-based planners such as RRT, RRT*, and RRT-Connect, the parent node of

a new sample is typically chosen based solely on Euclidean proximity or accumulated path cost, with no explicit constraint on directional continuity. Subsequent work has attempted to improve continuity by imposing curvature-related constraints—for example, by introducing fillet- or clothoid-based smoothing segments or by performing kinematic consistency adjustments on already generated trajectories (Yang *et al.*, 2024; Cao *et al.*, 2023; Liu *et al.*, 2024). These strategies, however, generally treat curvature as a post hoc correction applied after an edge has been added to the tree. As a result, sharp heading changes can still be introduced during tree growth, especially in tight environments.

To address this limitation, SR-RRT-APF introduces a curvature-aware nearest-node selection mechanism that embeds directional smoothness directly into the parent selection stage. The method linearly combines spatial proximity and heading continuity using a normalized weighting factor β_{curv}, which allows the planner to actively suppress high-angle turns during tree growth. This improves geometric continuity and, critically, improves executability in narrow aisles.

For each candidate sample $\tilde{x}$, the algorithm selects a parent node $x_i$from a local candidate-parent set by jointly considering spatial proximity and directional smoothness. Let $\theta_i$denote the angle between the incoming vector $\mathrm{parent}(i) \to x_i$ and the outgoing vector $x_i \to \tilde{x}$. The combined evaluation score is calculated as follows:

$$s_i = \frac{\|\tilde{x}-x_i\|^2-\min_j \|\tilde{x}-x_j\|^2}{\max_j \|\tilde{x}-x_j\|^2-\min_j \|\tilde{x}-x_j\|^2+\varepsilon} + \beta_{\mathrm{curv}} \frac{\theta_i-\min_j \theta_j}{\max_j \theta_j-\min_j \theta_j+\varepsilon}, \quad \text{(Eq. 15)}$$

where $\beta_{curv}$is the curvature weighting factor and $\varepsilon > 0$prevents division by zero.

Here, the indices $j$do not refer to all historical nodes in the search tree, but to the current candidate-parent subset used for parent selection. In implementation, this subset is formed by retaining only a limited number of nodes that are nearest to the candidate sample $\tilde{x}$. Therefore, the normalization terms $\min_j$ and $\max_j$ I n Eq. (15) are computed locally within the candidate-parent set, rather than over the entire tree. This design keeps the evaluation focused on the current expansion context and avoids unnecessary global computation. The parent node is then selected as the candidate with the minimum score s_i, which favors directionally continuous extensions while preserving local relevance in distance evaluation. For clarity, the normalized distance term and normalized angular term used in Eq. (15) are further written

separately as follows:

The parameters are set as $\beta_{\text{curv}} = 0.6$and $\varepsilon = 10^{-4}$. For clarity, the normalized distance term and normalized angular term used in Eq. (15) are further written separately as follows: The normalization process is defined as

$$d_i' = \frac{\|\tilde{x}-x_i\|^2 - \min_j \|\tilde{x}-x_j\|^2}{\max_j \|\tilde{x}-x_j\|^2 - \min_j \|\tilde{x}-x_j\|^2+\varepsilon}, \theta_i' = \frac{\theta_i - \min_j \theta_j}{\max_j \theta_j - \min_j \theta_j+\varepsilon}, \quad \text{(Eq. 16)}$$

and the combined evaluation score is calculated as

$$s_i = d_i' + \beta_{\text{curv}}\theta_i'。 \quad \text{(Eq. 17)}$$

As shown in Table 2, Node 2 is not the closest candidate in pure distance (1.40 m vs. 1.25 m for Node 1), but it exhibits a substantially smaller turning angle (30° vs. 50°). With $\beta_{curv} = 0.6$, Node 2 achieves the lowest combined score $s_2 = 0.24$and is therefore selected as the parent. This illustrates that the planner explicitly prefers directionally consistent parent nodes over purely nearest ones, thereby suppressing zigzag growth in narrow greenhouse aisles. The weighted formulation also provides a computationally efficient mechanism for jointly evaluating spatial proximity and directional smoothness during iterative tree expansion. Similar multi-factor evaluation strategies combining multiple criteria during node selection have been adopted in sampling-based motion planning algorithms (Karaman and Frazzoli, 2011; Huang *et al.*, 2025). In practice, the parameter β_{curv}controls the relative importance of curvature in the evaluation score. In this study, $\beta_{curv} = 0.6$ is selected to slightly favor directional smoothness while still maintaining sensitivity to spatial proximity, which was found empirically to produce stable and smooth tree growth in the tested greenhouse scenarios.

Table 2. Curvature-aware combined scores of different candidate parent nodes.

Node ID i	Distance $\|\tilde{x} - x_i\|$(m)	Turning angle θ_i(°)	Normalized distance	Normalized angle	Combined score s_i
1	1.25	50	0.00	0.71	0.43
2	1.40	30	0.19	0.29	0.24

3	1.75	70	0.63	1.00	0.82
4	2.00	20	1.00	0.00	0.50

Density-adaptive step length

After the parent node is determined, the expansion step length is modulated according to the local obstacle density $\rho(\tilde{x})$around the candidate sample.

Although the same density descriptor ρ(x̃) is also used in the sampling-guidance stage to bias the candidate sample through APF-based micro-adjustment, its role in the present step is different and therefore not redundant. In the sampling stage, the density term only affects the position of the candidate sample itself and is not conditioned on any parent node. In contrast, in the expansion stage, $\rho(\tilde{x})$is used after the parent node has been selected to regulate how far the tree extends from the selected parent toward the candidate sample. This yields a locally adaptive expansion rule in which the planner behaves conservatively in cluttered regions and extends more aggressively in open space, which is essential for maintaining feasibility in narrow greenhouse aisles and avoiding unnecessary collision checks. The step length is defined as

$$\eta_k = \frac{\eta_{\max}}{1+\alpha\,\rho(\tilde{x})} \in [\eta_{\min}, \eta_{\max}], \qquad \text{(Eq. 18)}$$

where $\alpha > 0$is a density-sensitivity coefficient that determines how strongly the expansion scale reacts to the surrounding obstacle distribution. A higher local density $\rho(\tilde{x})$ decreases η_k, preventing long, collision-prone jumps across multiple obstacles; in contrast, when $\rho(\tilde{x}) \approx 0$, the step length approaches η_{max}, enabling faster outward growth in relatively open corridors. When obstacles are dense, a larger $\rho(\tilde{x})$ causes η_k to automatically decrease, preventing invalid extensions that cross multiple obstacles. In open areas, where $\rho(\tilde{x}) \approx 0$, the step length approaches $\eta_{\max}$, thus improving exploration efficiency.

The local obstacle density can be obtained through neighborhood statistics, for example by counting obstacles within a radius R_ρ:

$$\rho(\tilde{x}) = \min\left(1, \frac{1}{N_{\max}} \sum_{i=1}^{N_{\text{obs}}} \mathbf{1}(\| c_i - \tilde{x} \| \leq R_\rho)\right), \quad \text{(Eq. 19)}$$

where $N_{\max}$is a normalization constant.$N_{\max}$ is chosen as the expected maximum number of obstacles that may appear within the neighborhood radius R_ρ, which provides a bounded normalization for the density estimate. Since the density is evaluated only from obstacles whose centers lie within the local neighborhood of $\tilde{x}$, the value of $\rho(\tilde{x})$reflects the local clutter level rather than the total number of obstacles in the global environment. Therefore, even when the environment contains a large number of obstacles overall, the normalization does not dilute the density estimate, and the adaptive step-length mechanism remains sensitive to local obstacle concentration.

The new node is then generated as

$$x_{\text{new}} = x_{\text{parent}} + \eta_k \frac{\tilde{x} - x_{\text{parent}}}{\|\tilde{x} - x_{\text{parent}}\|}. \quad \text{(Eq. 20)}$$

This adaptive step-length mechanism allows the planner to automatically regulate its expansion scale according to local structure, enhancing local feasibility in cluttered regions while maintaining high exploration efficiency in open corridors.

Figure 3a illustrates how high-density regions drive smaller η_k, preventing infeasible long segments, whereas low-density regions allow larger η_k, enabling rapid outward growth. In practice, this prevents the search tree from introducing unsafe, overly aggressive extensions in densely constrained greenhouse aisles and improves overall planning stability.

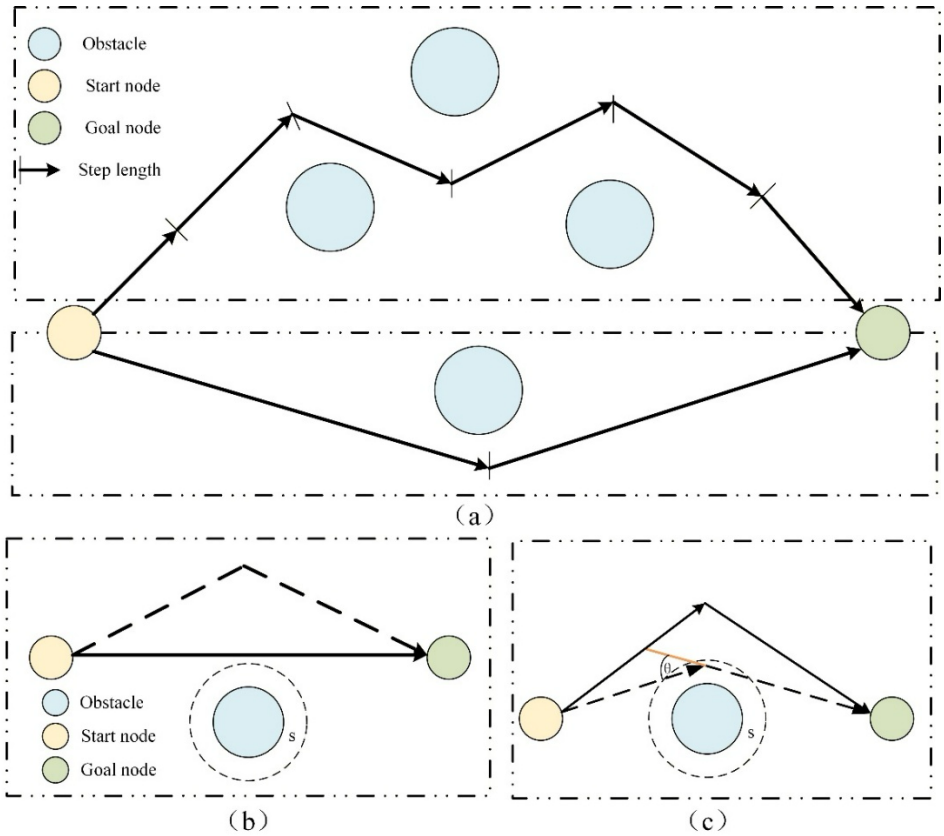

Figure 3. Density-adaptive step-length and safety-constrained smoothing mechanism.

Edge feasibility and goal connection

For each new edge $e = [x_{\text{parent}}, x_{\text{new}}]$, a unified geometric–safety dual criterion is applied to ensure path feasibility and safety:

$$\text{collision-free}(e) \wedge \min_{x \in e} d_{\min}(x) \geq \delta \qquad \text{(Eq. 21)}$$

where $d_{\min}(x) = \min_i(\| x - c_i \| - r_i)$, and δ denotes the safety margin determined by the combined envelope of the robot body and its payload (e.g., vegetable crates or pallets).

If the criterion is satisfied, the new node $x_{\text{new}}$is added to the tree. Furthermore, if $\| x_{\text{new}} - x_g \| < \eta_k$and the segment $[x_{\text{new}}, x_g]$also satisfies the dual criterion, the algorithm marks the state as "goal connected." This serves as the starting point for the least-cost path backtracking and safety-constrained post-processing procedures described in Section 3.3. Otherwise, the extension is discarded, and the algorithm returns to Section 3.1 for the next sampling attempt.

By enforcing the segment-level minimum-clearance constraint δduring tree generation rather

than after path formation, SR-RRT-APF converts safety checking from a heuristic post-processing task into a formal admissibility condition. This proactive constraint prevents boundary-skimming and near-collision behaviors from ever entering the search tree, thereby reducing redundant collision tests and ensuring that all accepted segments satisfy the predefined collision and clearance constraints during tree construction. The complete pseudocode for the core expansion mechanism is summarized in Table 3, which provides an overview of the generation–validation–connection workflow.

Table 3. Tree expansion with collision and clearance checking.

Algorithm 2
Input: $T, \tilde{x}, \beta_{\text{curv}}, \alpha, \eta_{min/max}, \delta$, world
Output: T, goal_connected
1. $i^* \leftarrow \text{argmin}_i\{s_i(\tilde{x}, x_i; \beta_{\text{curv}})\}$
2. $\rho \leftarrow$ local_obstacle_density$(\tilde{x})$
3. $\eta_k \leftarrow \text{clamp}(\frac{\eta_{\max}}{1+\alpha\cdot\rho}, \eta_{\min}, \eta_{\max})$
4. $x_{\text{new}} \leftarrow x_{\text{parent}}(i^*) + \eta_k \cdot \text{normalize}(\tilde{x} - x_{\text{parent}}(i^*))$
5. if collision_free$([x_{\text{parent}}, x_{\text{new}}])$ and min_clearance$([x_{\text{parent}}, x_{\text{new}}]) \geq \delta$ then
6. add x_{new} to T with parent $= i^*$
7. if $\|x_{\text{new}} - x_g\| < \eta_k$ and collision_free $([x_{\text{new}}, x_g])$ and min_clearance $([x_{\text{new}}, x_g]) \geq \delta$ then
8. goal_connected $\leftarrow$ True
9. end if
10. else
11. discard x_{new}
12. end if

Safety-constrained post-processing

After the expansion phase determines that a connection to the goal has been established, the

algorithm performs least-cost backtracking to extract the initial path, denoted as P_0. Although this path is generated to satisfy the minimum-clearance and curvature constraints, discretization effects and environmental complexity may still lead to local segments that are excessively close to obstacles or contain unnecessary bends.

To further enhance safety and geometric compactness without changing the global topology, SR-RRT-APF applies a lightweight safety-constrained refinement framework. In contrast to traditional smoothing methods—such as visibility-based optimization (Liu *et al.*, 2024), B-spline fitting (Yang *et al.*, 2024), or multi-objective waypoint optimization (Cao *et al.*, 2023)—which pursue curvature continuity as the primary goal, this framework explicitly prioritizes safety-margin maintenance under agricultural operational constraints (narrow aisles, dense obstacles, and large payload envelopes). Post-processing thus becomes a constraint-preserving refinement rather than a geometric beautification. The procedure consists of three coordinated components—minimum-clearance verification, shortcutting with clearance, and clearance-boosting push-away correction—that together guarantee both feasibility and simplicity.

(a) Minimum-clearance constraint

For any point $x$on the path, the minimum clearance is defined as before, and the following condition is strictly enforced throughout post-processing:

$$d_{\min}(x) \geq \delta \forall x \text{ on path}, \quad \text{(Eq. 22)}$$

where $\delta$is determined by the combined envelope of the robot body and its payload.

(b) Shortcutting with clearance

For any two points $x_i, x_j \in P_0$where $i+1 < j$, if the segment $[x_i, x_j]$satisfies both collision-free conditions and $\min_{x \in [x_i, x_j]} d_{\min}(x) \geq \delta$,the intermediate nodes are removed, and the two endpoints are directly connected. This operation eliminates redundant waypoints and shortens the geometric path length. In straight greenhouse aisles or repetitive back-and-forth segments, this procedure significantly reduces the number of kinks and improves motion efficiency. However, shortcutting may occasionally reduce the local obstacle clearance of some path segments. Therefore, a subsequent clearance-restoration step (push-away correction) is applied to ensure that the final trajectory satisfies the minimum safety margin.

(c) Clearance-boosting push-away

For internal points that still violate the clearance constraint after shortcutting, a small-step correction is applied along the outer normal of the nearest obstacle:

$$\Delta x = \kappa(\delta - d_{\min}(x))\, n(x), n(x) = \frac{x - c_{i^*}}{\|x - c_{i^*}\|}, x \leftarrow x + \Delta x, \quad \text{(Eq. 23)}$$

where $i^* = \arg\min_i(\| x - c_i \| - r_i)$identifies the nearest obstacle, and $\kappa > 0$ denotes the push-away gain. The correction step does not modify the start or goal points, and the adjusted path points are projected back into the workspace. The iteration continues until the entire path satisfies $d_{min} \geq \delta$, or until a predefined iteration limit is reached.

Table 4. Safety-constrained path refinement procedure.

Algorithm 3
Input: P_0 (path from findMinimumPath), δ, κ, trials, max_attempts
Output: P(safety-constrained path) or failure
1.$P \leftarrow P_0$
2.repeat trials times:
3. sample i, j such that $1 \leq i < j - 1 \leq \|P\|$
4.if collision_free$\left(\left[P[i], P[j]\right]\right)$ and min_clearance$\left(\left[P[i], P[j]\right]\right) > \delta$:
5. remove middle points from $P[i + 1..j - 1]$
6. for each internal vertex $x \in P$:
7. attempts←0
8. while $d_{\min}(x) < \delta$ and attempts < max_attempts:
9. $n \leftarrow \frac{x - c^*}{max(\|x - c^*\|, 1e-12)}$ #c^* is the closest obstacle center
10. $x \leftarrow x + \kappa \cdot (\delta - d_{\min}(x)) \cdot n$
11. increment attempts
12.if $\min_{x \in P} d_{\min}(x) \geq \delta$:
13.return P
14.else:return failure

Figure 3 b,c illustrates the two lightweight refinement operations: (b) clearance-constrained shortcutting that removes redundant nodes, and (c) normal-direction push-away correction that restores local safety margins. Together, these mechanisms maintain the path's global

connectivity while enlarging its minimum clearance and reducing unnecessary bends.

By embedding explicit safety constraints into every refinement step, SR-RRT-APF transforms post-processing from heuristic smoothing into a constraint-driven feasibility enhancement. The resulting path is both compact and collision-robust, requiring no further geometric optimization. The complete pseudocode of this refinement module is summarized in Table 4.

Algorithm simulation and analysis

To verify the effectiveness and robustness of the proposed SR-RRT-APF algorithm, comparative experiments were conducted in the MATLAB environment against several representative sampling-based planners, including the classical bidirectional planner RRT-Connect (Kuffner and LaValle, 2000), the improved AI-RRT* algorithm (Lin and Zhang, 2024), and a hybrid APF-RRT* planner (Ji *et al.*, 2025).

RRT-Connect served as the classical baseline due to its simplicity and high efficiency, while AI-RRT* and APF-RRT* -Ji were selected as representative enhanced variants emphasizing informed search and potential-field-guided planning, respectively. Together, these methods form a benchmark set that enables a more comprehensive evaluation of the safety–smoothness advantages of SR-RRT-APF.

The experiments were conducted under two benchmark settings. The first was a density-varying random-world benchmark in a 100 × 100 × 100 m^3 3D workspace, where the number of spherical obstacles was set to 5, 9, and 13 to represent different clutter levels. The second was a narrow-passage benchmark, in which obstacles were deliberately arranged to form a constrained passage for the robot. For all experiments, the start and goal states were fixed at $x_s = [5,5,5]$ and $x_g = [95,95,95]$, respectively, positioned near opposite corners of the workspace to ensure that the generated trajectories traverse the main spatial extent of the environment. Each algorithm was executed 30 independent runs under identical start–goal configurations and shared environments to ensure direct and fair comparison of path quality, computational efficiency, and safety-margin control under comparable conditions.

Four key performance indicators were selected for comparison: geometric path length (geom length), runtime, number of kinks, and minimum clearance (min-clearance). The kink threshold was set to $\theta_{th} = 25°$, which lies within the commonly used smoothness range (20°–30°)

reported in recent motion-planning studies. Liu *et al.* (2023) and Ren *et al.* (2025) indicated that constraining inter-node turning angles within this range can effectively reduce abrupt trajectory changes during execution.

The minimum-clearance threshold was set to $\delta = 0.03$ m, determined according to the robot's envelope size and sensor localization accuracy. Previous studies on mobile-robot and manipulator safety planning (Yan *et al.*, 2024; Liu *et al.*, 2023) suggest that a safety margin of approximately 20–40 mm is sufficient to prevent collision risks while maintaining feasible motion in cluttered environments.

Therefore, in this study, $\theta_{th} = 25°$ and $\delta = 0.03$ m were adopted as representative smoothness and safety parameters for the evaluation. These settings provide a consistent evaluation basis for comparing the safety-aware path planning performance of different algorithms in greenhouse-like environments.

In the first benchmark group, the four algorithms exhibited distinct path-generation characteristics under different obstacle densities. Representative trajectories are shown for visualization. As illustrated in Figure 4 a-c, the environments contain 5, 9, and 13 obstacles, respectively. In each subfigure, the trajectories are arranged from left to right as SR-RRT-APF, RRT-Connect, AI-RRT, and APF-RRT*-Ji-baseline.

Figure 5 and Table 5 summarize the statistical results obtained from 30 independent runs under identical experimental settings. SR-RRT-APF achieved shorter mean path lengths (approximately 165–186 m) than RRT-Connect (about 234–248 m) and maintained comparable performance to the APF-RRT*-Ji baseline. Although its runtime (0.08–0.17 s) was slightly higher than that of RRT-Connect in some cases, it remained significantly lower than AI-RRT* and APF-RRT*-Ji-baseline.

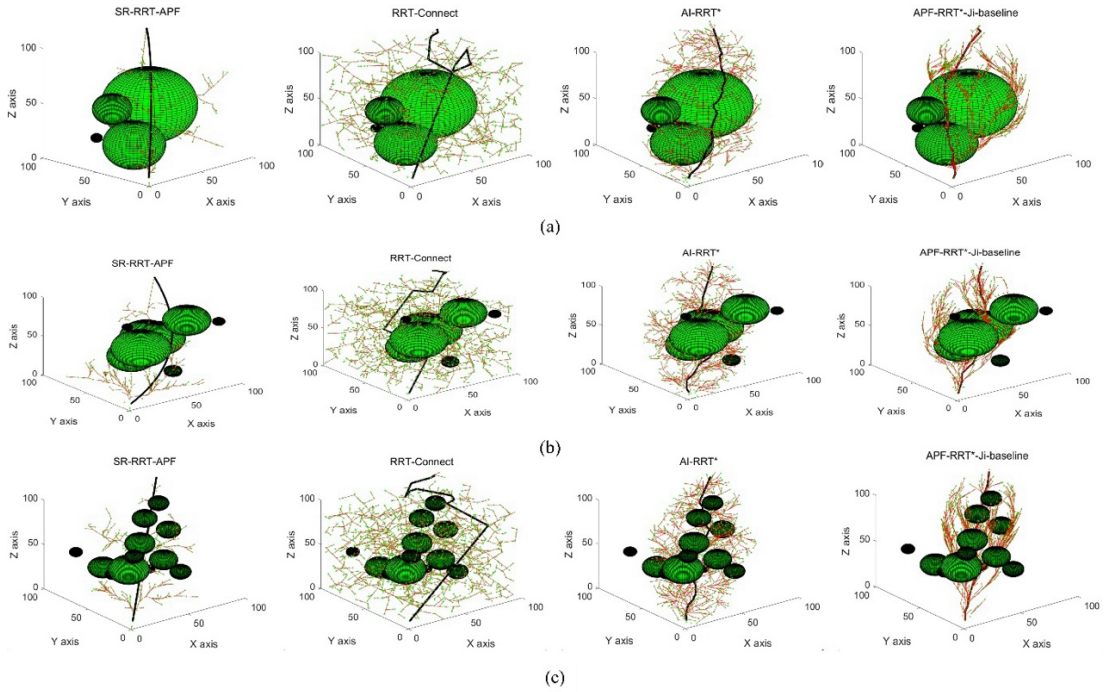

Figure 4. Representative path-planning results of four algorithms in 3D environments with different obstacle densities.

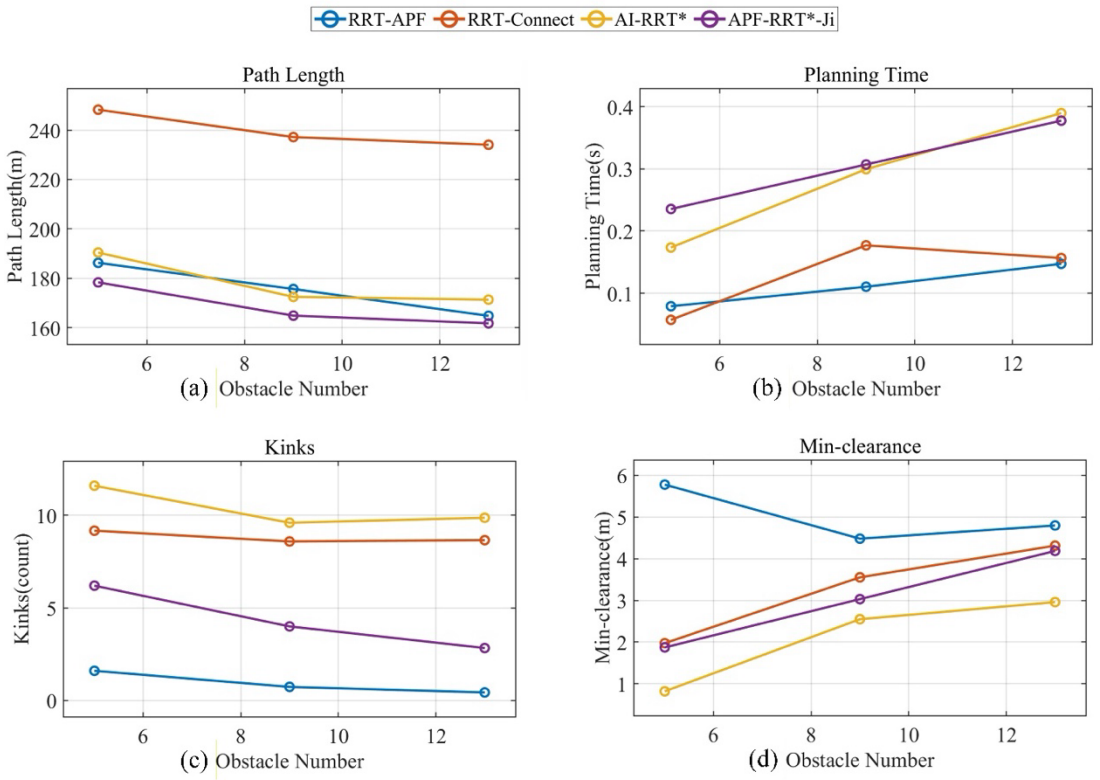

Figure 5. Representative single-run trajectories of four algorithms in a narrow 3D environment selected from 30 runs.

Table 5. Average results of four algorithms with 5, 9, and 13 obstacles (30 runs).

Obstacle Number	Metric	RRT-connect	AI-RRT *	APF-RRT*-Ji	SR-RRT-APF
5	Runtime (s)	0.057	0.173	0.235	**0.078**
	Geom length(m)	248.26	190.41	178.34	**186.26**
	Kinks (count)	9.17	11.60	6.20	**1.60**
	Min-clearance (m)	1.97	0.82	1.87	**5.78**
9	Runtime (s)	0.177	0.299	0.307	**0.110**
	Geom length(m)	237.19	172.46	164.89	**175.66**
	Kinks (count)	8.59	9.60	4.00	**0.73**
	Min-clearance (m)	3.55	2.55	3.03	**4.48**
13	Runtime (s)	0.157	0.390	0.378	**0.147**
	Geom length(m)	234.07	171.34	161.77	**164.80**
	Kinks (count)	8.66	9.87	2.83	**0.43**
	Min-clearance (m)	4.31	2.96	4.19	**4.80**

More importantly, SR-RRT-APF generated substantially smoother and safer trajectories, as reflected by both the significantly reduced number of kinks and the consistently larger obstacle clearances. The average number of kinks remained below 2 across all obstacle-density levels, while the other algorithms typically produced 6–12 turning points. At the same time, SR-RRT-APF maintained larger obstacle clearances, reaching about 5.78 m in the 5-obstacle case and remaining above 4 m in denser environments.

Overall, the results demonstrate that SR-RRT-APF achieves a favorable balance between computational efficiency, trajectory smoothness, and obstacle avoidance capability, thereby confirming its effectiveness for motion planning in obstacle-dense environments.

To further evaluate the algorithm's robustness in narrow greenhouse-like operating environments, additional experiments were conducted in a 3D narrow-passage scenario where obstacles were deliberately arranged to form a constrained corridor between the start and goal

regions. The evaluation metrics remained identical to those used in the previous experiments. In this scenario, the algorithms exhibited noticeably different path-generation behaviors. Figure 6 shows representative trajectories for visual comparison, panels a-d present the statistical results of thirty runs, corresponding to geometric path length, planning time, number of kinks, and minimum clearance, respectively. Table 6 summarizes the average values of these metrics for quantitative comparison.

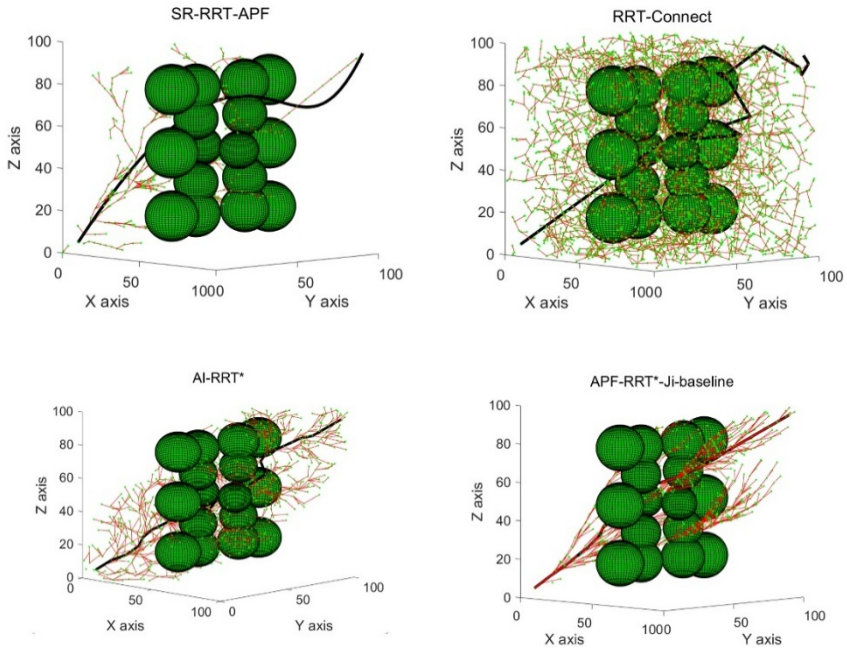

Figure 6. Representative single-run trajectories of four algorithms in a narrow 3D environment selected from 30 runs.

As shown in Figure 7 and Table 6, the four algorithms exhibit distinct planning characteristics under the same narrow-space constraint scenario. In terms of geometric path length, APF-RRT*-Ji produced the shortest average path (≈163.03 m), followed by AI-RRT* (≈175.82 m) and SR-RRT-APF (≈177.28 m), whereas RRT-Connect generated significantly longer trajectories (≈252.87 m). Although SR-RRT-APF did not achieve the shortest path, its results remained close to those of AI-RRT* and APF-RRT*-Ji while avoiding the excessive path length observed in RRT-Connect.

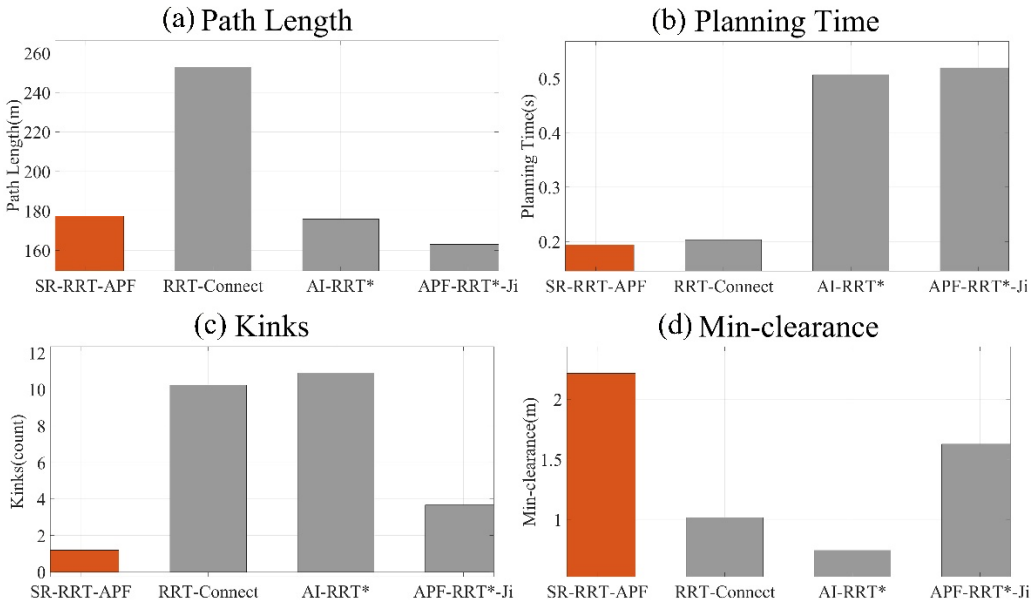

Figure 7. Performance comparison of four algorithms in a narrow and obstacle-constrained environment averaged over 30 runs.

Table 6. Average performance metrics of four algorithms in a narrow and obstacle-constrained environment over 30 runs.

Algorithm	RRT-connect	AI-RRT star	APF-RRT*-Ji	SR-RRT-APF
Runtime (s)	0.203	0.506	0.519	**0.194**
Geom length(m)	252.87	175.82	163.03	**177.28**
Kinks(count)	10.24	10.90	3.67	**1.20**
Min-clearance(m)	1.02	0.74	1.63	**2.22**

In terms of trajectory smoothness, SR-RRT-APF achieved the smallest number of kinks (≈1.20), compared with ≈3.67 for APF-RRT*-Ji and more than ten turning points for both RRT-Connect and AI-RRT*. Regarding safety margin, SR-RRT-APF also produced the largest minimum clearance (≈2.215 m), exceeding APF-RRT*-Ji (≈1.628 m), RRT-Connect (≈1.018 m), and AI-RRT* (≈0.744 m). In addition, SR-RRT-APF required an average runtime of ≈0.194 s, which is comparable to RRT-Connect (≈0.203 s) and noticeably lower than AI-RRT* (≈0.506 s) and APF-RRT*-Ji (≈0.519 s).

Overall, the results indicate that SR-RRT-APF maintains a favorable balance between trajectory smoothness, safety clearance, and computational efficiency in narrow and obstacle-constrained environments. Combined with the obstacle-density experiments (5, 9, and 13 obstacles), these results demonstrate that the proposed method consistently generates relatively smooth trajectories with stable safety margins while maintaining moderate planning cost across different environmental complexities.

Results

Prototype deployment experiments

To verify the practical feasibility of the robotic manipulation system and the overall task workflow in greenhouse crate-handling scenarios, prototype experiments were conducted on a self-developed agricultural composite mobile robot platform under representative operating conditions. The proposed SR-RRT-APF algorithm was quantitatively evaluated in a high-fidelity simulation environment constructed using the same workspace configuration as the physical platform, whereas the prototype experiments were used to assess system-level task execution under realistic operating conditions.

Figure 8 illustrates the experimental platform and workflow. Figure 8a presents the hardware configuration of the robot platform, including the mobile chassis, a six-degree-of-freedom robotic arm, the control unit, and the industrial PC. Figure 8b shows the overall system workflow. An RGB-D camera (Gemini335) first acquires image streams of the workspace, followed by RGB-D preprocessing and crate detection with pose estimation using an oriented bounding box (OBB)-based recognition method. The detected crate pose is then transformed into the robot base frame and used as the target for manipulator motion planning and execution. During operation, the handling process proceeds through four main stages—target recognition, path planning, grasp execution, and object placement—forming a continuous pick-and-place cycle. Figure 8c presents the ROS-based vehicle simulation used for system integration, and Figure 8d shows a representative camera recognition result obtained in the experiments. In the current prototype, the mobile chassis was manually teleoperated to the operating area rather than autonomously localized and navigated. Crate recognition was performed using RGB-D perception, from which the target position and orientation were extracted for grasp planning in

the manipulator workspace.

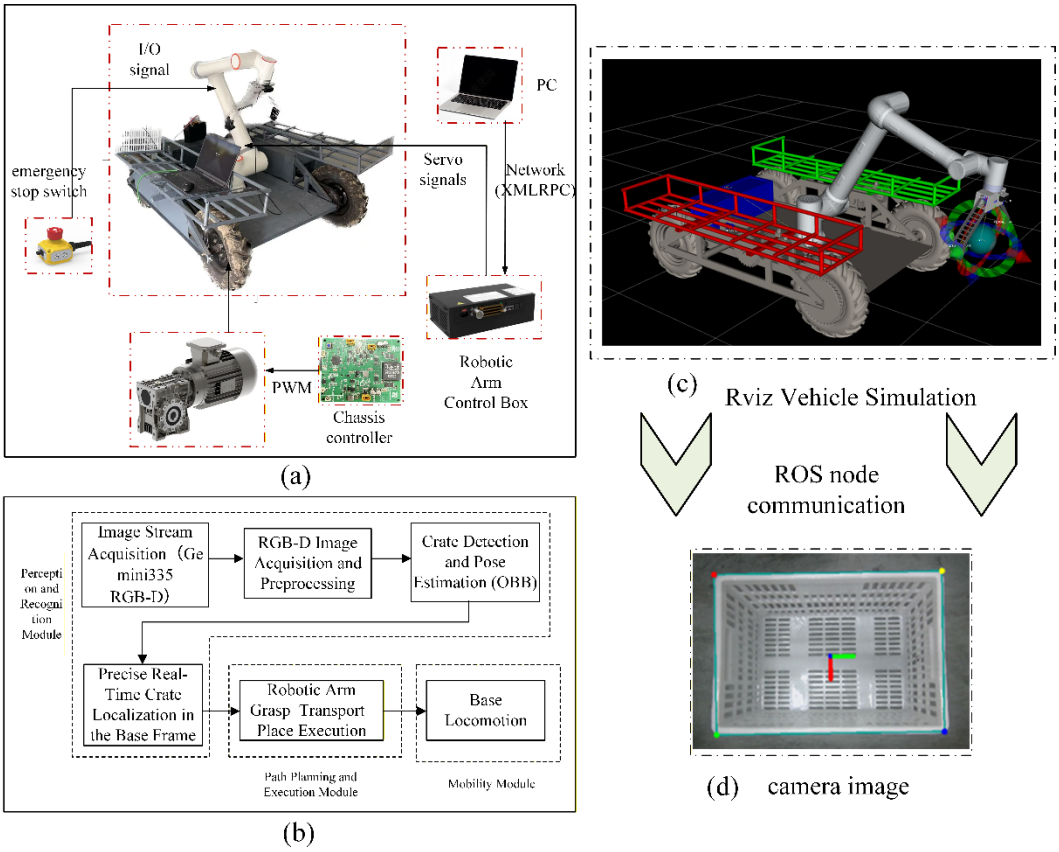

Figure 8. Overview of the experimental robotic platform and its perception–planning–execution framework used for real-world validation.

In the current prototype, the mobile chassis was manually teleoperated to the operating area rather than autonomously localized and navigated. Crate recognition was performed using RGB-D perception, from which the target position and orientation were extracted for grasp planning in the manipulator workspace. In the prototype demonstration, motion commands were executed by the onboard industrial controller, while the proposed SR-RRT-APF algorithm was evaluated separately in a high-fidelity simulation environment constructed using the same workspace configuration. This dual-track validation approach allowed the hardware experiments to verify mechanical coordination and system-level task feasibility, while the simulations quantitatively assessed the planning performance and trajectory characteristics of SR-RRT-APF under identical layouts.

The robot operated along two parallel greenhouse aisles with designated pickup and placement areas. The experimental site reflects typical greenhouse spatial conditions, including a 1.52 m aisle width, 0.25 m ridge height, and 1.10 m ridge spacing. Multiple vegetable crates were evenly arranged with a spacing of 0.8 m to emulate dense multi-target handling conditions (Figure 9). During the experiments, the robot was manually teleoperated to move to the designated working area rather than relying on fully autonomous navigation, since the soft and uneven greenhouse ground may reduce the reliability of autonomous navigation and precise positioning. After reaching the working area, the experiments focused on visual target recognition, crate pose extraction, and manipulator-level motion execution and task coordination under realistic operating conditions.

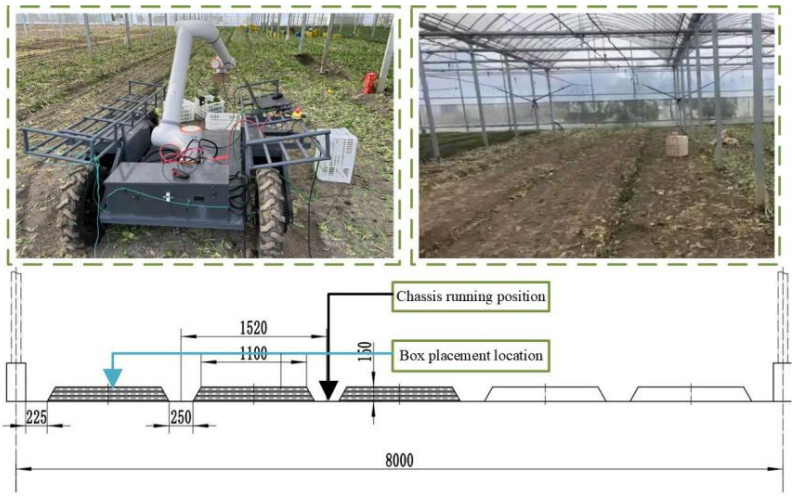

Figure 9. Robot operation path of the leafy vegetable harvesting robot.

This configuration allowed the task workflow and manipulation process to be evaluated under narrow and obstacle-rich greenhouse conditions, while the planning performance of SR-RRT-APF was quantitatively analyzed in simulation experiments using the same environment layout. The entire handling operation was organized in task units of “one vehicle handling ten crates.” After completing the handling of each target crate, the mobile chassis returned to its initial position and performed an in-place rotation to prepare for the next grasping cycle. The grasped crates were sequentially placed into fixed frame areas on both sides of the chassis to ensure structural stability and load safety during transportation.

To further evaluate the robustness of the robotic manipulation system under terrain-induced disturbances, a multi-angle disturbance experiment was designed, and the corresponding results are shown in Figure 10 a,b.

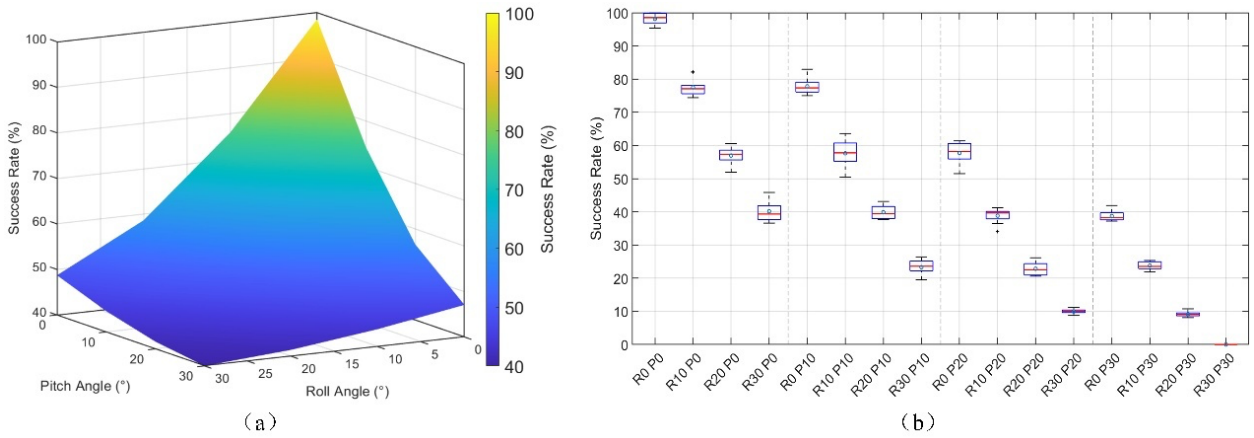

Figure 10. Experimental results of handling robustness.

This experiment aimed to assess the stability of grasping execution under different platform inclinations. The experimental platform simulated common greenhouse ground irregularities, such as soft-soil subsidence and small-slope undulations, by adjusting the roll (R) and pitch (P) angles within the range of 0°–30° in 10° increments, thereby forming 16 combined working conditions. Standardized vegetable crates were used as test objects, and a passive adaptive gripper was employed for grasping. Each condition was repeated ten times to statistically calculate the grasping success rate. Figure 10) illustrates the overall success-rate variation across different inclination combinations, whereas Figure 10b shows the statistical distribution of the repeated trials for each test condition.

Overall, the manipulation workflow remained feasible across most tested attitude combinations, indicating that the integrated perception–grasping–placement process retained acceptable robustness under moderate platform inclinations. Under low to moderate perturbations(e.g., R0–P0, R10–P10, R20–P10), the median success rate exceeded 85%, whereas the decline at larger inclinations was mainly associated with grasp alignment limitations of the end-effector

rather than online trajectory replanning behavior. When roll–pitch angles increased to severe levels (e.g., R30–P20, R30–P30), the success rate declined to 40–60 %, primarily due to gripper–crate misalignment caused by excessive platform inclination rather than path infeasibility.

These findings indicate that the task trajectories and manipulation workflow remain executable under moderate attitude disturbances, while the decline in success rate at large inclinations is mainly related to grasping alignment limitations of the end-effector.

The high task completion rate and consistent grasping performance demonstrate the practical feasibility of the proposed robotic handling system in uneven greenhouse terrain conditions characterized by soft soil subsidence and small ground undulations.

Discussion

The simulation results indicate that SR-RRT-APF achieves a strong balance among path efficiency, geometric smoothness, and environmental safety in dense and constrained planning environments, while the prototype experiments further support the system-level feasibility of the corresponding greenhouse manipulation workflow. Unlike conventional RRT-based planners that mainly address smoothness and safety after path generation, SR-RRT-APF incorporates curvature and clearance considerations directly into the tree-expansion process, thereby reducing the reliance on extensive post-generation correction. The multi-density and narrow-passage benchmarks further show that the proposed method can maintain larger safety clearances and fewer curvature discontinuities than the comparison planners. These properties are particularly relevant to robotic manipulation in narrow greenhouse aisles, where limited clearance and local path irregularities can significantly affect task execution.

Despite these advantages, several limitations remain:

(1) Computational efficiency. The integration of potential-field refinement and curvature-aware evaluation increases the per-iteration computational cost, which may limit applicability to high-frequency replanning or reactive control. Although the current runtime is acceptable for mid-scale agricultural tasks, further acceleration will still be needed for stricter real-time requirements.

(2) Parameter sensitivity. The planner depends on several manually tuned parameters, including

potential-field gains, curvature weights, and step-length coefficients. Their effective values may vary with obstacle density and workspace geometry, indicating the need for more adaptive or learning-assisted tuning strategies.

(3) Adaptation to dynamic environments. The current framework mainly assumes static or quasi-static obstacles. Extending SR-RRT-APF to dynamic scenarios will require tighter integration with online obstacle prediction, incremental replanning, or partial tree rewiring.

(4) Real-world deployment and long-term operation. In the current study, the SR-RRT-APF algorithm is primarily validated in simulation, while the physical prototype experiments focus on verifying system-level task feasibility. Integrating the proposed planner directly into the robotic control framework for real-time execution on the physical platform remains an important step for future work. In large-scale or long-duration greenhouse operations, additional factors—such as sensor drift, model deviation, and mechanical wear—may further influence system performance. Coupling SR-RRT-APF with online calibration, perception filtering, and fault-tolerant control will therefore be essential for sustained reliability.

The experimental observations also suggest broader practical implications. First, the consistency between simulated path characteristics and observed system behavior indicates that curvature-aware and clearance-aware planning principles are compatible with greenhouse-oriented manipulation workflows. Second, the multi-angle disturbance experiments show that most task failures were caused not by infeasible paths but by gripper–crate misalignment under extreme roll–pitch conditions, implying that future improvements should strengthen the integration of motion planning with perception compensation and adaptive grasp execution. Overall, SR-RRT-APF provides a meaningful step toward connecting constrained-space path planning with practical greenhouse robotic manipulation, although its full potential will depend on further progress in adaptive parameterization, dynamic replanning, and tighter system-level integration.

Conclusions

This study presented SR-RRT-APF, a safety-refined path-planning method motivated by greenhouse crate-handling scenarios and intended for robotic operation in narrow and obstacle-dense workspaces. By integrating scheduled goal-bias sampling, curvature-aware parent-node

selection, density-adaptive expansion, and clearance-aware trajectory refinement, the proposed method improves path smoothness and environmental safety during the planning process rather than relying solely on extensive post-generation smoothing or correction.

Simulation results under multiple obstacle-density configurations and a narrow-passage benchmark showed that SR-RRT-APF consistently produced trajectories with fewer turning points and larger minimum obstacle clearances than RRT-Connect, AI-RRT*, and APF-RRT*-Ji in the tested benchmark settings, while maintaining competitive computation time. In particular, the proposed method reduced path length by approximately 25–30% relative to RRT-Connect in dense and constrained environments and showed clear advantages in trajectory smoothness and clearance preservation.

Prototype experiments on the self-developed agricultural robot platform further demonstrated the system-level feasibility of the associated perception–manipulation workflow under greenhouse crate-handling conditions. Although the quantitative planning evaluation was conducted in a matched high-fidelity simulation environment rather than through direct real-time deployment on the physical manipulator controller, the experimental results support the practical compatibility of the proposed planning strategy with greenhouse-oriented robotic manipulation tasks. Future work will focus on tighter integration of perception, real-time motion planning, and more autonomous system-level execution in complex field environments.

Data and Materials Availability

All data generated or analyzed during this study are available from the corresponding author upon reasonable request.

Competing Interests

The authors declare that they have no competing interests.

Authors' Contributions

HHX conceived the study, developed the SR-RRT-APF algorithm, and drafted the manuscript. ZCY supervised the research, revised the manuscript, and contributed to data interpretation. All authors read and approved the final version of the manuscript.

References

Ahmad J, Zhang Y, Chen H, 2025. Enhancing the safety and smoothness of path planning. Expert Syst Appl 259:120420.

Bian Y, Zhang Q, Guo R, 2023. BPFPS-RRT: An improved bidirectional RRT algorithm based on penalty function and potential field. Sensors 23:3901.
Cao N, Liu J, Zhang Q, 2023. A multi-objective path-smoothing algorithm based on node adjustment and turn smoothing. Meas Control 56:123–134.
Chen Y, Zhang Y, Liu L, et al, 2022. Path planning of the fruit tree pruning manipulator based on improved RRT-Connect algorithm. Int J Agric Biol Eng 15:177-188.
Feng Z, Zhou L, Qi J, Hong S, 2024. DBVS-APF-RRT*: A global path planning algorithm with ultra-high-speed initial path generation and high optimal path quality. Expert Syst Appl 249:123571.
Gammell JD, Barfoot TD, Srinivasa SS, 2022. Informed RRT*: Optimal sampling-based path planning focused via direct sampling of an admissible ellipsoidal heuristic. Auton Robots 46:1-18.
Gao G, Guo H, Zhang J, Zhang Z, Wu T, Lu H, et al., 2023. An efficient headland-turning navigation system for a safflower-picking robot. J Agric Eng 54:1539.
Guan T, Zhang X, Li Y, 2025. An improved artificial potential field with RRT star algorithm. Sci Rep 15:694.
Guo Y, 2025. Structural design, modelling and simulation analysis of a cage broiler inspection robot. J Agric Eng 56:1806.
He X, Wang H, Zhang D, Ji H, 2025. Improved RRT*-Connect manipulator path planning in a narrow environment with multiple obstacles. Sensors 25:2364.
Huang S, Wang J, Liu X, 2025. Multi-strategy bidirectional RRT*: Enhanced sampling and local optimization for motion planning in complex environments. Sci Rep 15:13915.
Huang Y, Jiang W, Xu S, 2025. A multi strategy bidirectional RRT* algorithm for efficient mobile robot path planning. Sci Rep 15:29501.
Ji H, Wang C, Wang C, et al, 2025. Motion planning for hyper-redundant manipulator systems: combining path following and improved APF-RRT* Path finding. Complex Intell Syst 11:441.
Kuffner JJ, LaValle SM, 2000. RRT-Connect: An efficient approach to single-query path planning. Proc IEEE Int Conf Robot Autom, pp. 995-1001.
Karaman S, Frazzoli E, 2011. Sampling-based algorithms for optimal motion planning. The international journal of robotics research 30, 846-894.
Li Y, Ma S, 2023. Navigation of apple tree pruning robot based on improved RRT-Connect algorithm. Agriculture 13:1495.
Lin J, Wu Y, Chen X, 2023. UAV path planning using bi-directional APF-RRT* in complex environments. Expert Syst Appl 213:119137.
Lin Y, Zhang Y, 2024. AI-RRT*: An improved Quick Informed-RRT* algorithm with hybrid bidirectional search and adaptive adjustment. Intell Serv Robot 17: 357-372.
Liu H, Li J, Yang F, Shen Y, 2024. Fast path planning for kinematic smoothing of robotic manipulator motion. IEEE Access 12:21574-21586.
Liu S, Wang H, Chen Q, et al, 2024. Kinematic-constrained RRT algorithm with post waypoint

shift for the shortest path planning of wheeled mobile robots. Sensors (Basel) 24:6948.
Liu Y, Fu Z, Sun D, 2023. Motion planning for agricultural manipulators in unstructured greenhouse environments. Comput Electron Agric 209:107816.
Liu Y, Wang X, Sun Y, 2023. Path planning techniques for mobile robots: Review and challenges. Expert Syst Appl 224:119951.
Lu M, Gao H, Dai H, Lei Q, Liu C, 2024. Path tracking and curvature-constrained hybrid A algorithm for autonomous agricultural vehicles. Agriculture 14:2043.
Rajendran V, Nair GP, Yu Y, et al, 2024. Towards autonomous selective harvesting: A review of robot perception, design, motion planning and control. J Field Robot 41:1753-1796.
Ran K, Wang Y, Zhao H, et al, 2024. Improved RRT path-planning algorithm based on the Clothoid. Sensors (Basel) 24: 7812.
Ren Z, Kang Y, Yang L, Jia H, Wang S, 2025. Optimization algorithm for 3D smooth path of robotic arm in Dynamic Obstacle Environments. Appl Sci 15:2116.
Sun Y, Yi K, 2023. Agricultural machinery photoelectric automatic navigation control system based on back-propagation neural network. J Agric Eng 54:1530.
Swedeen J, Droge G, Christensen R, 2023. Fillet-based RRT: A rapid convergence implementation of RRT* for curvature-constrained vehicles. J Intell Robot Syst 108:68.
Wang W, Zhao H, Li P, 2024. AODA-PF-RRT*: Artificial potential field with obstacle density awareness for improved RRT* path planning. Electronics 13:2573.
Wei P, Peng C, Lu W, Zhu Y, Vougioukas S, Fei Z, Ge Z, 2025. Efficient and safe trajectory planning for autonomous agricultural vehicle headland turning in cluttered orchard environments. IEEE Robot Autom Lett 10:2574-2581.
Xiao X, 2024. AC-YOLO: Citrus detection in the natural environment of orchards. J Agric Eng 55:1654.
Yan W, Zhou H, Luo S, 2024. A safe heuristic path-planning method based on a search strategy. Sensors (Basel) 24:101.
Yang J, Wu X, Li Z, 2024. An analytical tool path smoothing algorithm for robotic machining. Comput Ind Eng 192:108576.
Zhang B, Wang H, Yin M, 2025. Hybrid path planning algorithm for underactuated AUV based on directional cone and goal-biased dynamic artificial potential field. Sci Rep 15:11500.
Zhang H, Liu J, Chen M, 2025. Integration of improved artificial potential field and RRT algorithms for efficient manipulator path planning. Meas Control 58:1-12.
Zhang X, Liu Y, Sun J, Wang Z, 2024. RRT-APF path planning algorithm for mobile robots in complex environments. Electronics 13:4963.
Zhao D, Zhang C, Zhang H, 2022. Collision-free path planning for greenhouse robots under narrow-row constraints. Biosyst Eng 221:30–42.
Zhong H, Cong M, Wang M, Du Y, Liu D, 2024. HB-RRT: A path planning algorithm for mobile robots using Halton sequence-based rapidly-exploring random tree. Eng Appl Artif Intell 133:108362.

Zhu Z, Yuan C, Zhou P, 2024. Development of a combined-harvester navigation control system based on visual SLAM–inertial guidance fusion. J Agric Eng 55:1583.